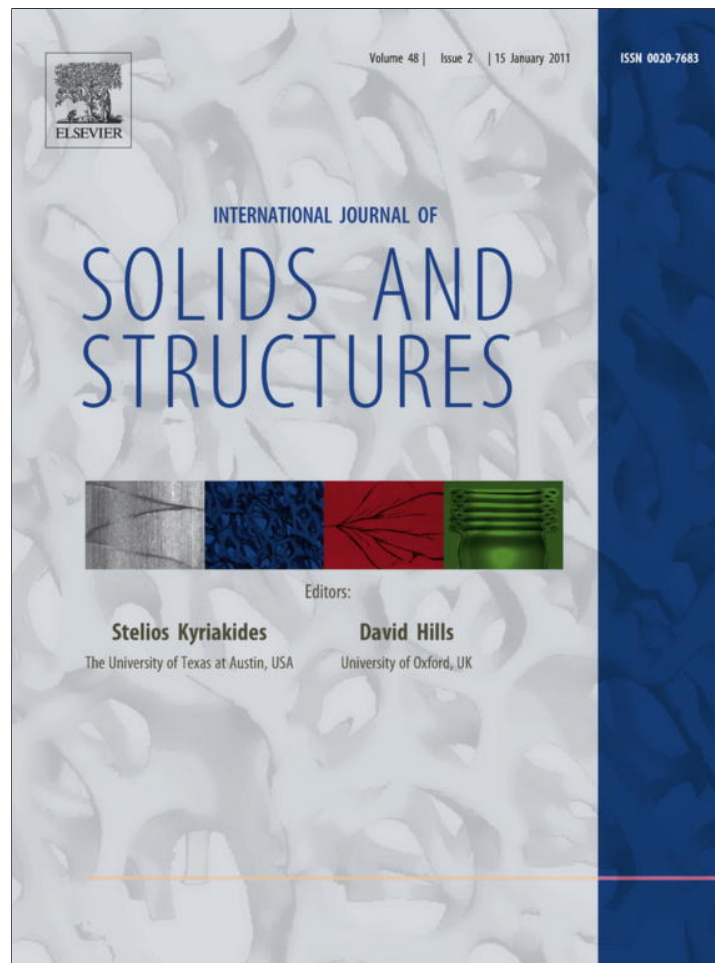


Provided for non-commercial research and education use.  
Not for reproduction, distribution or commercial use.

\*\*\*Download is permitted to HPC-Lab members and for educational purposes only\*\*\*



This article appeared in a journal published by Elsevier. The attached copy is furnished to the author for internal non-commercial research and education use, including for instruction at the authors institution and sharing with colleagues.

Other uses, including reproduction and distribution, or selling or licensing copies, or posting to personal, institutional or third party websites are prohibited.

In most cases authors are permitted to post their version of the article (e.g. in Word or Tex form) to their personal website or institutional repository. Authors requiring further information regarding Elsevier's archiving and manuscript policies are encouraged to visit:

<http://www.elsevier.com/copyright>



ELSEVIER

Contents lists available at ScienceDirect

## International Journal of Solids and Structures

journal homepage: [www.elsevier.com/locate/ijssolstr](http://www.elsevier.com/locate/ijssolstr)

## Plane-strain discrete dislocation plasticity incorporating anisotropic elasticity

Siamak Soleymani Shishvan<sup>a,b,1</sup>, Soheil Mohammadi<sup>b</sup>, Mohammad Rahimian<sup>b</sup>, Erik Van der Giessen<sup>c,\*</sup><sup>a</sup> Faculty of Civil Engineering, University of Tabriz, P.O. Box 51666-16471, Tabriz, Iran<sup>b</sup> Department of Structural Engineering, School of Civil Engineering, University of Tehran, P.O. Box 11365-4563, Tehran, Iran<sup>c</sup> Zernike Institute for Advanced Materials, Department of Applied Physics, University of Groningen, Nyenborgh 4, 9747 AG, Groningen, The Netherlands

## ARTICLE INFO

## Article history:

Received 2 August 2010

Received in revised form 30 September 2010

2010

Available online 12 October 2010

## Keywords:

Discrete dislocation plasticity (DDP)

Anisotropic elasticity

Size effects

Thin films

## ABSTRACT

The increasing application of plane-strain testing at the (sub-) micron length scale of materials that comprise elastically anisotropic cubic crystals has motivated the development of an anisotropic two-dimensional discrete dislocation plasticity (2D DDP) method. The method relies on the observation that plane-strain plastic deformation of cubic crystals is possible in specific orientations when described in terms of edge dislocations on three effective slip systems. The displacement and stress fields of such dislocations in an unbounded anisotropic crystal are recapitulated, and we propose modified constitutive rules for the discrete dislocation dynamics of anisotropic single crystals. Subsequently, to handle polycrystalline problems, we follow an idea of O'Day and Curtin (J. Appl. Mech. 71 (2004) 805–815) and treat each grain as a plastic domain, and adopt superposition to determine the overall response. This method allows for a computationally efficient analysis of micro-scale size effects. As an application, we study freestanding thin copper films under plane-strain tension. First, the computational framework is validated for the special case of isotropic thin films modeled by means of a standard 2D DDP method. Next, predictions of size dependent plastic behavior in anisotropic columnar-grained thin films with varying thickness/grain size are presented and compared with the isotropic results.

© 2010 Elsevier Ltd. All rights reserved.

## 1. Introduction

Understanding mechanical size effects has become a central topic in materials science and engineering due to the recent trend of miniaturization in numerous technological applications, e.g. MEMS. Among various mechanisms leading to a strong size dependency in micro-scale crystalline solids, the most known and well-explored sources are plastic strain gradient, geometrically necessary dislocations and constraints/freedoms on motion/nucleation of dislocations due to grain boundaries/free surfaces or any other internal interfaces. Conventional continuum plasticity is length-scale independent and is based on the concept of homogeneous deformation, precluding size effects, thus inappropriate to solve micro-scale problems accurately. On the other hand, a micro-scale problem is too large for fully atomistic modeling, while small enough that individual dislocation effects are important and cannot be averaged into a classical continuum plasticity constitutive law. Although many attempts have been made to reproduce size effects in nonlocal plasticity theories (e.g. Fleck and Hutchinson, 2001; Gurtin, 2002; Acharya and Bassani, 2000), an alternative

technique, the discrete dislocation dynamics has effectively captured micro-scale size dependency.

The discrete dislocation plasticity (DDP) adopts a continuum description of the elastic lattice and retains individual dislocations as carriers of plastic deformation. DDP has received a significant area of applications after development of the superposition method by Van der Giessen and Needleman (1995) for solving a boundary value problem (BVP). In such a DDP framework, long-range interactions between dislocations are directly accounted for through their linear elastic fields, while short-range phenomena, including dislocation motion, nucleation, annihilation and pinning at obstacles, are incorporated through constitutive rules. Although the framework is fully three dimensional, it has been used mostly in solving two dimensional plane-strain BVPs. Past studies include the analysis of micro-scale plasticity near cracks (e.g. Cleveringa et al., 2000; O'Day and Curtin, 2004; Deshpande et al., 2002) or indenter tips (e.g. Widjaja et al., 2005, 2007) and investigations of microstructural size effects in bulk (Cleveringa et al., 1997; Balint et al., 2008; Guruprasad et al., 2008) and thin film materials (Nicola et al., 2003, 2005b; Shishvan and Van der Giessen, 2010; Shishvan et al., 2010).

By construction, DDP describes anisotropic plasticity, as defined by the available slip systems in the crystal, but so far all applications have assumed elastic isotropy. However, real crystals are anisotropic and it remains unclear how important this is. The

\* Corresponding author. Tel.: +31 50 363 8046; fax: +31 50 363 4886.

E-mail address: [E.van.der.Giessen@rug.nl](mailto:E.van.der.Giessen@rug.nl) (E. Van der Giessen).<sup>1</sup> Visiting scholar, Zernike Institute for Advanced Materials, Department of Applied Physics, University of Groningen, The Netherlands.

importance of elastic anisotropy for short-range dislocation interactions, such as junctions, has been emphasized in the literature; this issue is beyond of the scope of this paper and readers are referred to Rhee et al. (2001) and references therein. At a larger length scale, the inhomogeneous stress distribution in polycrystalline metal thin films caused by variations in texture was investigated by Baker et al. (2001). Accordingly, Rajagopalan et al. (2008) claimed that the Bauschinger effect seen in their aluminium films could partly be the result of such texture induced stress variations. The objective of this paper, therefore, is to develop the elastically anisotropic version of DDP, yet limited to 2D plane-strain problems. The anisotropic elasticity theory of dislocations is available in the literature (e.g. Bacon et al., 1980; Hirth and Lothe, 1982) in terms of Green's functions. Several attempts (Rhee et al., 2001; Han et al., 2003) have been made to develop anisotropic 3D DD simulation programs, but these suffer from the very slow computational speed due to the lack of closed-form solution of the Green's function in anisotropic media. A significant step forward is the very recent proposal by Yin et al. (2010), but in view of the interest in plane-strain analyses and the much higher computing speeds achievable there, we confine our attention to a 2D DDP method.

The paper is organized as follows. After a brief summary of anisotropic elasticity, we start out with a recap of Rice (1987)'s conditions under which plane strain plastic deformation of a cubic crystal can be represented by straight edge dislocations on three effective slip systems. In particular orientations, we can thus apply the closed-form expressions of the displacement and stress fields of straight edge dislocations given by Hirth and Lothe (1982) in a 2D DDP method, as described in Section 3. While the superposition method of Van der Giessen and Needleman (1995) can be directly employed for a single crystal, we advance the superposition framework developed by O'Day and Curtin (2004) for the analysis of polycrystalline samples, which has the added benefit of being very efficient computationally. After due modification of the constitutive rules to account for elastic anisotropy, the method is demonstrated in Section 4 by simulating Cu thin films in tension. With an anisotropy ratio of 3.21, Cu is among the most anisotropic of metals; the results are expected to reveal the strongest effect of anisotropy. First, by assuming isotropic medium, the computational approach is validated against results of the standard DDP method on plane-strain tension of thin films. Then, size dependent stress-strain curves as well as the Bauschinger effect are predicted for anisotropic polycrystalline thin films of varying thickness/grain size, and then compared with the isotropic results. The method brings an auxiliary advantage of studying the linear elastic behavior of thin films, augmented with a simple experimental fitting of the plane-strain elastic modulus.

## 2. Anisotropic elasticity and plane-strain plasticity of crystals

Linear elastic behavior of a crystal is governed by Hooke's law in the form  $\sigma_{ij} = C_{ijkl}\varepsilon_{kl}$  or its inverse  $\varepsilon_{ij} = S_{ijkl}\sigma_{kl}$ , where  $C_{ijkl}$  and  $S_{ijkl}$  are the components of the stiffness and compliance tensors. For cubic crystals, there are only three independent elastic constants, namely  $c_{11}$ ,  $c_{12}$  and  $c_{44}$ . When adopting base vectors that coincide with the cubic axes, this cubic anisotropy is reflected in the following non zero elements  $C_{iii} = c_{11}$ ,  $C_{ijj} = c_{12}$  and  $C_{ijij} = c_{44}$  for  $i \neq j$  (no summation over repeated indices). The elastic constants in an arbitrary coordinate system are obtained by straightforward transformation rules.

While elastic anisotropy is defined by symmetries in the atomic lattice, plastic anisotropy of single crystals arises from the fact that plastic deformation in a crystal occurs by the creation and motion of dislocations on specific discrete slip systems. The slip system of

a dislocation is determined by the crystallographic plane on which the dislocation exists and by the direction of slip which the dislocation induces in the crystal. In an FCC crystal, 12 slip systems exist which are denoted as  $\{111\}\langle 110 \rangle$ , with  $\{111\}$  corresponding to the family of slip planes and  $\langle 110 \rangle$  to the family of slip directions.

It is known (Rice, 1987) that in a single FCC crystal, the simultaneous action of certain slip systems gives rise to plane-strain deformations (see also Kysar et al. (2005)). This is illustrated in Fig. 1 for a state of plane-strain deformation in the  $[101]-[010]$  plane. The  $(\bar{1}11)[101]$  and  $(11\bar{1})[101]$  slip systems can be combined to form what Rice (1987) called a 'complex slip system'. This effective in-plane slip system acts in the  $[101]$  direction and is referred to in this paper as the slip system (i) (see Fig. 1b). The  $(\bar{1}\bar{1}\bar{1})[110]$  and  $(\bar{1}\bar{1}\bar{1})[011]$  slip systems operate in equal amounts to form an effective plane-strain slip system on the  $(\bar{1}\bar{1}\bar{1})$  plane in the  $[121]$  direction; this is referred to as slip system (ii). Similarly, the slip system (iii) is the effective plane-strain slip system on the  $(111)$  plane and in the  $[\bar{1}2\bar{1}]$  direction as a combination of  $(111)[\bar{1}10]$  and  $(111)[01\bar{1}]$ . The relative in-plane angles between the slip systems as shown in Fig. 1b read (i)–(ii):  $54.736^\circ$ ; (ii)–(iii):  $70.528^\circ$  and (i)–(iii):  $-54.736^\circ$ .

Consistent with the plane-strain condition, straight edge dislocations perpendicular to the plane of consideration can be introduced (the  $z$  axis being parallel to the dislocation line). It is noted that, by geometry, the effective lengths of the Burgers vectors are  $b$ ,  $\sqrt{3}/2b$  and  $\sqrt{3}/2b$  for the three slip systems (i), (ii) and (iii), respectively (Kysar et al., 2007; Wang et al., 2009).

### 2.1. Edge dislocations

According to the classical analysis of Eshelby et al. (1953) the solution of the elastic fields of a long straight dislocation is considerably simplified when the dislocation line is normal to a plane of symmetry, so that certain components of the elastic modulus tensor vanish. Supposing the dislocation line to be along one of a triad of orthonormal axes, such a condition is satisfied if either (a) one axis is an axis of sixfold symmetry, or (b) each axis is an axis of evenfold symmetry (Hirth and Lothe, 1982). In an FCC crystal, dislocation lines along  $\langle 101 \rangle$  are indeed consisted in this category. This can be easily seen by transformation of the elastic tensor to the plane-strain coordinate system. For the coordinate system  $x-y$  of Fig. 1b, where the plane of consideration is  $(\bar{1}01)$ , Hooke's law in contracted notation reads:

$$\begin{Bmatrix} \sigma_{xx} \\ \sigma_{yy} \\ \sigma_{zz} \\ \sigma_{yz} \\ \sigma_{xz} \\ \sigma_{xy} \end{Bmatrix} = \begin{bmatrix} c'_{11} & c'_{12} & c'_{13} & 0 & 0 & 0 \\ c'_{12} & c'_{22} & c'_{12} & 0 & 0 & 0 \\ c'_{13} & c'_{12} & c'_{33} & 0 & 0 & 0 \\ 0 & 0 & 0 & c'_{44} & 0 & 0 \\ 0 & 0 & 0 & 0 & c'_{55} & 0 \\ 0 & 0 & 0 & 0 & 0 & c'_{66} \end{bmatrix} \begin{Bmatrix} \varepsilon_{xx} \\ \varepsilon_{yy} \\ \varepsilon_{zz} \\ 2\varepsilon_{yz} \\ 2\varepsilon_{xz} \\ 2\varepsilon_{xy} \end{Bmatrix}, \quad (1)$$

where the primed moduli are defined by the cubic moduli through

$$\begin{aligned} c'_{11} &= c'_{33} = \frac{1}{2}(c_{11} + c_{12} + 2c_{44}), \\ c'_{22} &= c_{11}, \\ c'_{12} &= c_{12}, \\ c'_{13} &= \frac{1}{2}(c_{11} + c_{12} - 2c_{44}), \\ c'_{44} &= c'_{66} = c_{44}, \\ c'_{55} &= \frac{1}{2}(c_{11} - c_{12}). \end{aligned} \quad (2)$$

It is noted that  $c'_{14} = c'_{15} = c'_{24} = c'_{25} = c'_{34} = c'_{35} = c'_{46} = c'_{56} = 0$ , which means that the elastic field is separable into a plane-strain part and an anti-plane-strain part; or, in dislocation language, the

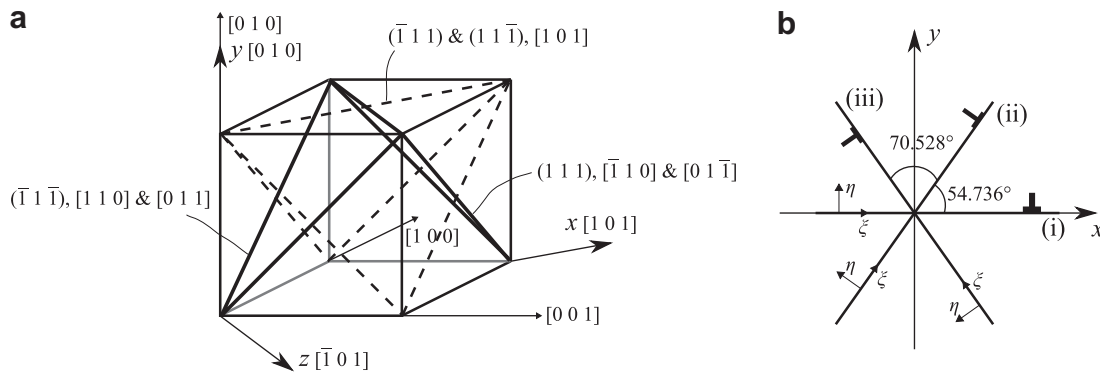


**Fig. 1.** (a) An FCC crystal in the cubic coordinate system with simultaneously active slip systems to resemble the plane-strain condition in the [101]–[010] plane and (b) the plane-strain state of the FCC crystal: coordinate system  $x$ – $y$  with three effective slip systems, and the local coordinate system  $\xi$ – $\eta$ .

edge and screw components are separable. Furthermore, by  $c'_{16} = c'_{26} = c'_{36} = c'_{45} = 0$ , the fields can be expressed analytically in a simple closed forms.

For an edge dislocation line located at the origin of the  $x$ – $y$  coordinate system and parallel to the  $z$  axis, with a Burgers vector  $\mathbf{b} = [b_x, b_y, 0]^T$ , the displacement field is given by (Hirth and Lothe, 1982):

$$\begin{aligned}
 u_x(x, y) &= \frac{b_x}{4\pi} \left( \tan^{-1} \frac{2xy\lambda \sin \varphi}{x^2 - \lambda^2 y^2} + \frac{\bar{c}'_{11} - c'^2_{12}}{2\bar{c}'_{11} c'_{66} \sin 2\varphi} \ln \frac{q}{t} \right) \\
 &\quad + \frac{b_y}{4\pi \lambda \bar{c}'_{11} \sin 2\varphi} \left[ (\bar{c}'_{11} - c'_{12}) \cos \varphi \ln qt - (\bar{c}'_{11} + c'_{12}) \right. \\
 &\quad \left. \times \sin \varphi \tan^{-1} \frac{x^2 \sin 2\varphi}{\lambda^2 y^2 - x^2 \cos 2\varphi} \right], \\
 u_y(x, y) &= -\frac{\lambda b_x}{4\pi \bar{c}'_{11} \sin 2\varphi} \left[ (\bar{c}'_{11} - c'_{12}) \cos \varphi \ln qt - (\bar{c}'_{11} + c'_{12}) \right. \\
 &\quad \left. \times \sin \varphi \tan^{-1} \frac{y^2 \lambda^2 \sin 2\varphi}{x^2 - \lambda^2 y^2 \cos 2\varphi} \right] \\
 &\quad + \frac{b_y}{4\pi} \left( \tan^{-1} \frac{2xy\lambda \sin \varphi}{x^2 - \lambda^2 y^2} - \frac{\bar{c}'_{11} - c'^2_{12}}{2\bar{c}'_{11} c'_{66} \sin 2\varphi} \ln \frac{q}{t} \right), \quad (3)
 \end{aligned}$$

with

$$\begin{aligned}
 \lambda &= (c'_{11}/c'_{22})^{1/4}, \\
 \bar{c}'_{11} &= (c'_{11} c'_{22})^{1/2}, \\
 \varphi &= \frac{1}{2} \cos^{-1} \frac{c'^2_{12} + 2c'_{12} c'_{66} - \bar{c}'^2_{11}}{2\bar{c}'_{11} c'_{66}}, \\
 q^2 &= x^2 + 2xy\lambda \cos \varphi + y^2 \lambda^2, \\
 t^2 &= x^2 - 2xy\lambda \cos \varphi + y^2 \lambda^2.
 \end{aligned} \quad (4)$$

Appendix A discusses the need for careful consideration of the branch cut in the arctan function appearing in Eq. (3) for the displacement discontinuity.

The corresponding stress field reads:

$$\begin{aligned}
 \sigma_{xx} &= -\frac{M b_x}{2\pi \rho^4 c'_{22}} \left\{ [(\bar{c}'_{11} - c'_{12})(\bar{c}'_{11} + c'_{12} + 2c'_{66}) - \bar{c}'_{11} c'_{66}] y x^2 + \frac{\bar{c}'^2_{11} c'_{66}}{c'_{22}} y^3 \right\} \\
 &\quad - \frac{M b_y c'_{66}}{2\pi \rho^4} \left( \frac{c'_{11}}{c'_{22}} x y^2 - x^3 \right), \\
 \sigma_{yy} &= \frac{M b_x c'_{66}}{2\pi \rho^4} \left( y x^2 - \frac{\bar{c}'_{11}}{c'_{22}} y^3 \right) \\
 &\quad + \frac{M b_y}{2\pi \rho^4 \bar{c}'_{11}} \left\{ [(\bar{c}'_{11} - c'_{12})(\bar{c}'_{11} + c'_{12} + 2c'_{66}) - \bar{c}'_{11} c'_{66}] x y^2 + c'_{22} c'_{66} x^3 \right\}, \\
 \sigma_{xy} &= \frac{M b_x c'_{66}}{2\pi \rho^4} \left( x^3 - \frac{\bar{c}'_{11}}{c'_{22}} x y^2 \right) - \frac{M b_y c'_{66}}{2\pi \rho^4} \left( \frac{c'_{11}}{c'_{22}} y^3 - y x^2 \right), \quad (5)
 \end{aligned}$$

where  $M$  is a modulus pre-factor and  $\rho$  an effective distance, defined as

$$\begin{aligned}
 M &= (\bar{c}'_{11} + c'_{12}) \left[ \frac{\bar{c}'_{11} - c'_{12}}{c'_{22} c'_{66} (\bar{c}'_{11} + c'_{12} + 2c'_{66})} \right]^{1/2}, \\
 \rho^4 &= \left( x^2 + \frac{\bar{c}'_{11}}{c'_{22}} y^2 \right)^2 + \frac{(\bar{c}'_{11} + c'_{12})(\bar{c}'_{11} - c'_{12} - 2c'_{66})}{c'_{22} c'_{66}} x^2 y^2. \quad (6)
 \end{aligned}$$

These fields can be used in a DDP framework instead of the well-known isotropic ones:

$$\begin{aligned}
 \sigma_{xx} &= \frac{-E}{4\pi(1-\nu^2)} \left[ b_x \frac{y(3x^2 + y^2)}{(x^2 + y^2)^2} + b_y \frac{x(y^2 - x^2)}{(x^2 + y^2)^2} \right], \\
 \sigma_{yy} &= \frac{E}{4\pi(1-\nu^2)} \left[ b_x \frac{y(x^2 - y^2)}{(x^2 + y^2)^2} + b_y \frac{x(3y^2 + x^2)}{(x^2 + y^2)^2} \right], \\
 \sigma_{xy} &= \frac{E}{4\pi(1-\nu^2)} \left[ b_x \frac{x(x^2 - y^2)}{(x^2 + y^2)^2} - b_y \frac{y(y^2 - x^2)}{(x^2 + y^2)^2} \right], \quad (7)
 \end{aligned}$$

where  $E$  is Young's modulus and  $\nu$  is Poisson's ratio of the medium.

As a first comparison between anisotropic and isotropic fields, Fig. 2 shows the variation of the shear stress,  $\sigma_{\xi\eta}$ , resolved on the local  $\xi$ – $\eta$  coordinate system (cf. Fig. 1b) at its origin due to a dislocation at  $(\xi, \eta = 10b)$ . In this figure, the elastic constants (of Cu) are chosen as  $c_{11} = 168.4$ ,  $c_{12} = 121.4$  and  $c_{44} = 75.4$  GPa for the anisotropic fields in Eq. (5) and the commonly used values of

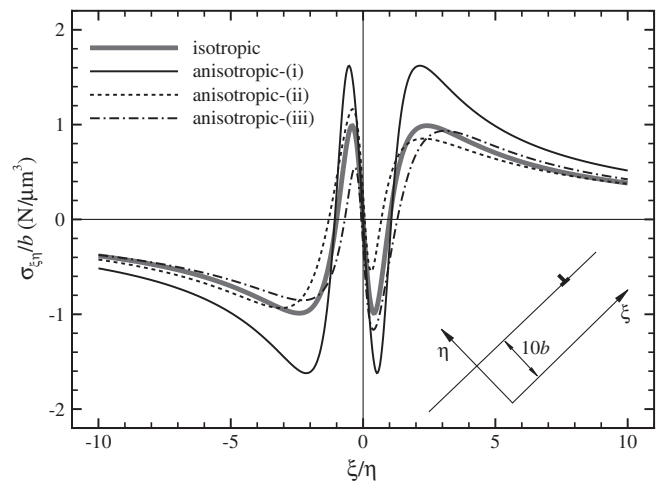


**Fig. 2.** Shear stress at the origin due to a dislocation located at  $(\xi, \eta)$ . See Fig. 1 for definitions of (i), (ii) and (iii) slip systems and the local coordinate system  $\xi$ – $\eta$ . Effective values of Burgers vector lengths are used for anisotropic calculations.

$E = 110$  GPa and  $\nu = 0.34$  for the isotropic solution (7). It should be noted, however, that the idea of an elastically isotropic crystal is an idealization of a real anisotropic crystal and that this approximation is not unique. We argue that the most appropriate values are those averaged over all possible orientations of the coordinate system relative to the crystal axes. Either averaging of the elastic constants  $C_{ijkl}$  (Voigt average) or of the elastic compliances  $S_{ijkl}$  (Reuss average) is possible; the former is appropriate for a polycrystal in which the grains have the same state of strain, while the latter is better suited for identically stressed grains. For Cu, the Voigt average leads to:  $E = 144.6$  GPa and  $\nu = 0.324$  while the Reuss average results in:  $E = 110.0$  GPa and  $\nu = 0.369$  (Hirth and Lothe, 1982).

In Fig. 2 an asymmetric profile of the resolved shear stresses are observed for slip systems (ii) and (iii), which is expected due to anisotropy. As a consequence the interaction with another edge dislocation on the same slip system is asymmetric in relative position. Accordingly the equilibrium positions of two dislocations on slip systems (ii) and (iii) are not symmetric, as shown in Fig. 3b and c. On slip system (i) the equilibrium positions of two dislocations are symmetric, as seen in Fig. 3a, but the mutual angles are different from the well-known ones  $-45^\circ$ ,  $90^\circ$  and  $135^\circ$ — in an isotropic solid. This issue can be useful in the modeling of dislocation walls, where anisotropy introduces different configurations for dislocations in the wall according to the slip system.

Another way of demonstrating the difference in long-range fields of dislocations in an anisotropic crystal compared to an isotropic one is by studying the interaction in a dipole. This is shown in Fig. 4 by plotting the dependence of the resolved shear stress due to a dipole on the size of the dipole,  $L_{\text{dipole}}$ . It is seen from this figure that elastic anisotropy enhances the induced shear stress compared to the isotropic case. For slip systems (ii) and (iii) the increase is around 5% independent of  $L_{\text{dipole}}$  but for slip system (i) it is as large as 32%. As a consequence the interactions between the dislocations is stronger, which ultimately will affect the glide velocity of dislocations, the back stress on sources and the length of pile-ups on that slip plane. In order to find out how large the effect of anisotropy is, we will now employ the above fields in anisotropic discrete dislocation plasticity.

### 3. Discrete dislocation formulation

The framework of discrete dislocation plasticity (DDP), originally derived by Van der Giessen and Needleman (1995), can be used to determine the quasi-static evolution of deformation and stress states of a dislocated solid subjected to an arbitrary prescribed loading. Following Kubin et al. (1992), the approach is incremental in time; i.e. the dislocation structure and the stress state are assumed to be known at a given instant, and then by prescribing an increment of loading (i) the deformation and stress state are updated, and (ii) the evolution of the dislocation structure is computed. The long-range interactions being captured by the

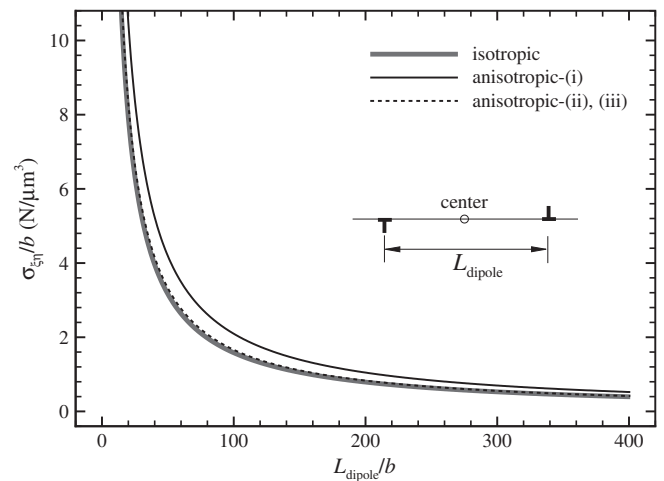


Fig. 4. Shear stress at the center of a dipole versus the dipole size for anisotropic vis-a-vis isotropic cases. Slip systems (i), (ii) and (iii) and their local coordinate system  $\xi$ - $\eta$  are defined in Fig. 1. The anisotropic results are based on the effective magnitudes of the Burgers vector, being  $b$ ,  $\sqrt{3}/2b$  and  $\sqrt{3}/2b$  respectively. The isotropic calculation is based on  $E = 110$  GPa and  $\nu = 0.34$ .

linear elastic fields as presented above, the short-range interactions are incorporated through a set of constitutive rules, which govern dislocation motion, nucleation, annihilation and interaction with point obstacles.

Each time step involves three main computational stages: (i) determining the Peach–Koeher force acting on all dislocations; (ii) determining the rate of change of the dislocation structure, caused by motion of dislocations, generation of new dislocations, their mutual annihilation, and their possible pinning at obstacles; and (iii) determining the stress and strain states for the updated dislocation arrangement.

Superposition is the key idea for determining the deformation and stress states of a dislocated solid. The singular stress and strain fields of dislocations given analytically in the previous section apply to an infinite medium. For a finite body with prescribed boundary conditions, the actual fields are written as the sum of the singular fields associated with the individual dislocations and a non-singular image field that enforces the boundary conditions. The solution of the latter can be obtained by one of the available numerical methods for solving elasticity problems, such as the finite element method.

Implementation of anisotropy for a single crystal is rather straightforward. For a polycrystalline body, however, the superposition method of Van der Giessen and Needleman (1995) suffers from the fact that the elastic properties are not homogeneous, so that the elastic singular fields cannot be applied. In principle, this can be accounted for by polarization stresses as introduced in

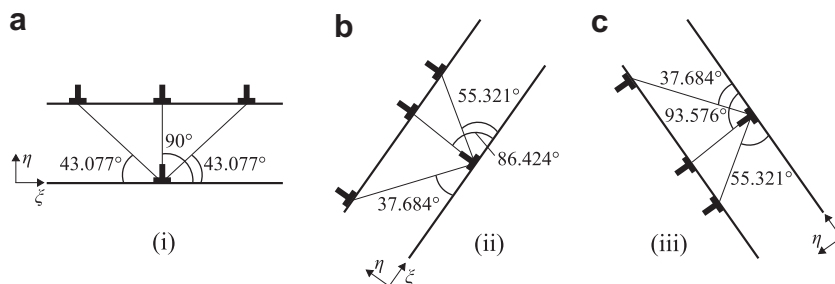


Fig. 3. Stable positions of edge dislocations in an anisotropic medium (Cu moduli), where the dislocation line is parallel to  $(101)$  direction, for the slip systems (a) i, (b) ii and (c) iii.

(Van der Giessen and Needleman, 1995), but this would be an enormous computational burden. Instead, we propose to adopt the superposition framework of O'Day and Curtin (2004).

### 3.1. Formulation of BVPs in Polycrystalline Solids

The superposition framework of O'Day and Curtin (2004) for solving a BVP for a polycrystalline solid is depicted schematically in Fig. 5. Restricting attention to small displacement gradients, the governing equations to be satisfied at any time  $t$  read:

$$\frac{\partial \sigma_{ij}}{\partial x_j} = 0, \quad \varepsilon_{ij} = \frac{1}{2} \left( \frac{\partial u_i}{\partial x_j} + \frac{\partial u_j}{\partial x_i} \right), \quad \sigma_{ij} = \bar{L}_{ijkl} \varepsilon_{kl}, \quad (8)$$

supplemented with boundary conditions in terms of displacements or tractions  $T_i$ , on the parts  $S_u$  and  $S_f$  of the polycrystalline body, respectively. In (8), the moduli  $\bar{L}_{ijkl}$  are different for each grain, and depend on their orientation (see Appendix B). As illustrated in Fig. 5a, the BVP is solved by the superposition of DD sub-problems subject to 'generic' boundary conditions and a fully elastic sub-problem subject to all actual boundary conditions. As the latter is solved here by the finite element method, it is referred to as the FE sub-problem. Each grain is treated as a separate potentially plastic region, and described by a DD sub-problem to be constructed subsequently. Once the FE and DD sub-problems are solved, linearity of the governing Eq. (8) allows the solution to the actual BVP to be written as their superposition,

$$u_i = u_i^{DD} + u_i^{FE}, \quad \sigma_{ij} = \sigma_{ij}^{DD} + \sigma_{ij}^{FE}, \quad \varepsilon_{ij} = \varepsilon_{ij}^{DD} + \varepsilon_{ij}^{FE}. \quad (9)$$

Following O'Day and Curtin (2004), the generic boundary conditions of the DD sub-problems are chosen as  $U_i^{DD} = 0$  and  $T_i^{DD} = 0$  on  $S_u$  and  $S_f$ , respectively, as shown in Fig. 5a. Additionally,  $U_i^{DD} = 0$  is pre-

scribed on the boundary  $S_b$  between the grains. Thus, the only information about the full problem that is used in the solution of a DD sub-problem is the geometry of the plastic region and the knowledge of whether displacement or traction boundary conditions are applied on boundaries shared by the DD sub-problem and the full problem. The incremental solution of the DD sub-problem is then obtained from the superposition of an infinite space dislocation problem and a corrective problem, just like in (Van der Giessen and Needleman, 1995): summation of the singular fields associated with individual dislocations in an infinite domain and a non-singular image field that enforces the DD sub-problem boundary conditions (see Fig. 5b). Thus, the solution of the DD sub-problem can be written as

$$u_i^{DD} = \tilde{u}_i + \hat{u}_i, \quad \sigma_{ij}^{DD} = \tilde{\sigma}_{ij} + \hat{\sigma}_{ij}, \quad \varepsilon_{ij}^{DD} = \tilde{\varepsilon}_{ij} + \hat{\varepsilon}_{ij}, \quad (10)$$

where  $(\sim)$  denotes the sum of the fields of individual dislocations, i.e.,

$$\tilde{u}_i = \sum_I u_i^{(I)}, \quad \tilde{\sigma}_{ij} = \sum_I \sigma_{ij}^{(I)}, \quad \tilde{\varepsilon}_{ij} = \sum_I \varepsilon_{ij}^{(I)} \quad (I = 1, \dots, N). \quad (11)$$

Here,  $N$  is the number of dislocations in the DD sub-problem for each grain. The  $(\wedge)$  fields are the fields to correct for the actual boundary conditions on  $S^{DD}$ . An outcome of the solution of the DD sub-problems is a traction  $T_i^*$  along the appropriate boundary  $S_b$ , which will be used in the FE sub-problem.

The FE sub-problem models the entire domain as an elastic intact medium subject to all global boundary conditions. Information of the plastic deformation in each plastic region is transmitted to the remainder of the domain through the addition of an internal traction force  $-T_i^*$  along  $S_b$  in the FE sub-problem. The internal traction  $T_i^*$  comprises the interface tractions of the DD sub-problems along the common grain boundary (GB). The governing equations of the FE sub-problem are linear and can thus be solved very

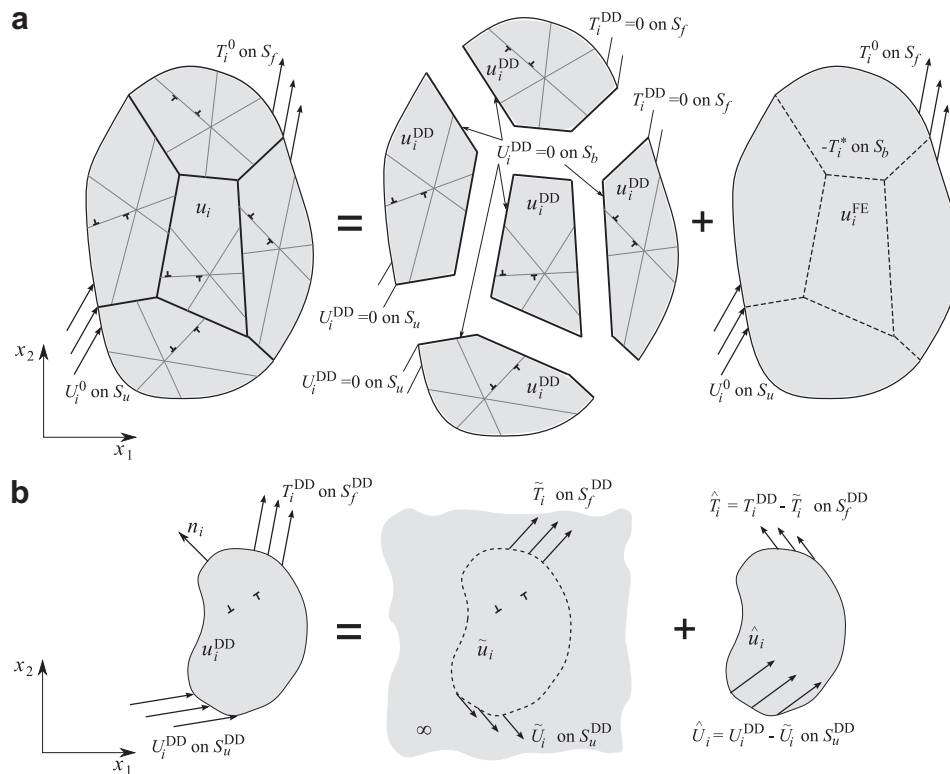


**Fig. 5.** Schematic representation of boundary conditions and details of the superposition principle in the present DDP method for polycrystals. (a) The desired problem is decomposed into two supplemental problems: a set of DD sub-problems subject to generic boundary conditions and an FE sub-problem correcting for the desired boundary conditions and incorporating the interaction between grains. (b) Standard superposition framework used to solve each DD sub-problem by decomposition into the problem of interacting dislocations in the infinite solid ( $\tilde{}$  fields) and the complementary problem for the grain without dislocations ( $\hat{}$  fields).

quickly because the formation and inversion of the overall stiffness matrix needs to be done only once at the beginning of the computations.

It should be noted that the FE sub-problem influences the dislocation structure and its evolution because the Peach-Koehler force is calculated on each dislocation using the full field obtained from (9) and (10). The glide component of the Peach-Koehler force on dislocation  $l$  is expressed as

$$f^{(l)} = m_i^{(l)} \left( \hat{\sigma}_{ij} + \sum_{j \neq i} \sigma_{ij}^{(j)} + \sigma_{ij}^{FE} \right) b_j^{(l)}, \quad (J = 1, \dots, N), \quad (12)$$

with  $b_j^{(l)}$  its Burgers vector and  $m_i^{(l)}$  the slip plane normal. This force being a configurational force, it governs the evolution of the dislocation structure.

### 3.2. Constitutive rules for dislocation dynamics

Constitutive rules for dislocation dynamics are usually based on those proposed by Kubin et al. (1992), and in 2D particularly those accounted for in (Van der Giessen and Needleman, 1995). In the following, they are summarized and modified with necessary adaptations for the present anisotropic framework.

The glide component of the Peach-Koehler force on dislocation  $l$  ( $f^{(l)}$  in Eq. (12)) controls its glide velocity  $v^{(l)}$  through the drag law

$$v^{(l)} = \frac{f^{(l)}}{B}, \quad (13)$$

where  $B$  is the drag coefficient.

The Peach-Koehler force also controls the nucleation of dislocations by a 2D representation of the Frank-Read (F-R) source, as a point that generates a dipole of edge dislocations when the Peach-Koehler force at the source exceeds the source strength  $b\tau_{nuc}$  during a time span  $t_{nuc}$  (Van der Giessen and Needleman, 1995). The sign of the dipole is determined by the direction of Peach-Koehler force at the position of source. The distance between dislocations of the generated dipole,  $L_{nuc}$ , is chosen in such a way that the total shear stress on the slip plane,  $\tau$ , balances the attractive shear stress that the two dislocations exert on each other. According to Eq. (5) and after insertion of the minimum value  $\tau_{nuc}$  for  $\tau$ , the value of  $L_{nuc}$  can be calculated. For slip system (i), this is straightforward because the value of the resolved shear stress is defined from Eq. (5)<sub>3</sub> (for  $\xi = L_{nuc}$  and  $\eta = 0$ , i.e.  $x = L_{nuc}$  and  $y = 0$ ) as

$$L_{nuc}^{(i)} = \frac{Mc'_{66} b}{2\pi \tau_{nuc}}. \quad (14)$$

For slip systems (ii) and (iii), the calculated resolved shear stress (for  $\xi = L_{nuc}$  and  $\eta = 0$ , i.e.  $x = L_{nuc}/\sqrt{3}$  and  $y = \sqrt{2/3}L_{nuc}$ ) leads to

$$L_{nuc}^{(ii)} = L_{nuc}^{(iii)} = \frac{M(\frac{2}{3}A_1 - A_2)}{2\pi A_3} \frac{\sqrt{3} b}{\tau_{nuc}}, \quad (15)$$

where

$$\begin{aligned} A_1 &= [(\bar{c}'_{11} - c'_{12})(\bar{c}'_{11} + c'_{12} + 2c'_{66}) - \bar{c}'_{11}c'_{66}] \left( \frac{2}{\bar{c}'_{11}} + \frac{1}{c'_{22}} \right) + c'_{66} \left( \frac{c'_{22}}{\bar{c}'_{11}} + 2\frac{c'_{11}}{c'_{22}} \right), \\ A_2 &= c'_{66} \left( 1 - 2\frac{\bar{c}'_{11}}{c'_{22}} \right), \\ A_3 &= \left( 1 + 2\frac{\bar{c}'_{11}}{c'_{22}} \right)^2 + 2\frac{(\bar{c}'_{11} + c'_{12})(\bar{c}'_{11} - c'_{12} - 2c'_{66})}{c'_{22}c'_{66}}. \end{aligned} \quad (16)$$

Annihilation of two dislocations with opposite signed Burgers vectors occurs when they come within a material-dependent critical annihilation distance  $L_e$  (say,  $6b$ ) of each other.

## 4. Application to thin films

Extensive research during the last two decades has convincingly shown that the plastic response of a thin film depends not only on the grain size, just as in bulk polycrystalline materials, but also on the film thickness. Experimental results in combination with theoretical/numerical modeling have led to the view that the grain size dependence of yield strength is governed by the same mechanisms as in bulk (i.e. the Hall-Petch effect) and is coupled to the thickness dependence. Possible mechanisms responsible for these size effects include: piling-up of dislocations against GBs; thickness dependence of the mean-free dislocation path; and source limitation in case of very thin films. All these size effects are captured by DDP models and have been a source for validation of various non-local crystal plasticity theories, e.g., Nicola et al. (2005a), Limkumnerd and Van der Giessen (2008), Liu et al. (2010).

The two-dimensional DDP method has been used to systematically investigate the plastic behavior of thin films (Nicola et al., 2003, 2005b, 2006; Kumar et al., 2009; Shishvan and Van der Giessen, 2010; Shishvan et al., 2010), and has led to a quantitative description of size dependency. Although these studies have adopted simple isotropic elasticity, remarkable agreement with experiments has been achieved. However, one may wonder what the influence of crystal anisotropy is on the response of strongly textured polycrystalline thin films. To study this, the present method is employed to investigate the mechanical behavior of unpassivated freestanding thin films, with due attention for the overall linear elastic behavior, size dependent plastic behavior and the Bauschinger effect. The computational advantages of the present method are demonstrated as well. But before presenting the results, the general methodology presented in Section 3 is refined for a thin film with the underlying material model.

### 4.1. 2D DDP model of thin films

Polycrystalline columnar-grained thin films of thickness  $h$  are modeled as two dimensional arrays of rectangular grains with a uniform grain size  $d$ , as illustrated in Fig. 6. Plane-strain conditions are assumed normal to the  $x_1 - x_2$  plane. Each grain has three slip systems, with slip planes oriented at  $\phi$ ,  $\phi + 54.736^\circ$  and  $\phi + 125.264^\circ$  from the loading direction (see Fig. 1b). Note that  $\phi$  in this case is the angle between the slip system (i) and the tensile direction which is coincide with  $x_1$  axis. The orientation of each grain,  $\phi$ , is different for all grains and chosen randomly with a uniform distribution. Parallel planes in a slip system are spaced at a distance of  $100b \sim 200b$ . All GBs are assumed to be impenetrable to dislocations, while dislocations can freely leave through the top and bottom surfaces since they are unpassivated. Sources are randomly distributed over the potentially active slip planes with a given density  $\rho_{nuc}$ , and the value of  $\tau_{nuc}$  of each source is determined randomly from a distribution corresponding to different lengths of the segments forming an F-R source in three dimensions. As an extension of the 2D source model in Van der Giessen and Needleman (1995), a 2D constitutive rule to represent F-R sources has recently been introduced by Shishvan and Van der Giessen (2010) which takes into account that the grain size limits the available and effective dislocation source length and thereby its strength. In this model, the value of  $\tau_{nuc}$  of each source is determined by

$$\tau_{nuc} = \tau_{nuc}^0 + \tau_{nuc}^{LN}, \quad (17)$$

where  $\tau_{nuc}^0$  is a material constant and the value of  $\tau_{nuc}^{LN}$  is selected randomly from a log-normal distribution. This distribution is bounded by the theoretical strength of material and by a minimum strength that depends on the film thickness and the grain size. The

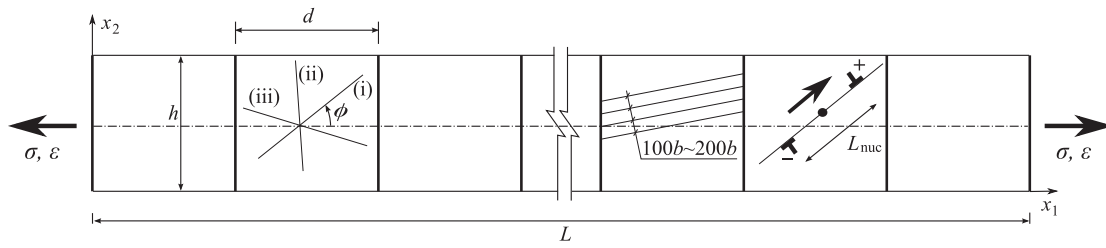


Fig. 6. Plane-strain model of a columnar-grained thin film with thickness  $h$  and grain size  $d$ , illustrating slip systems, slip planes and a source.

value of  $\tau_{nuc}^0$  along with the density of sources  $\rho_{nuc}$ —free parameters of the model— have to be fitted to an experimental stress–strain curve for a film of a specific thickness and grain size. The method has been successfully applied to predict the stress–strain curves for two independent sets of Cu films (Xiang and Vlassak, 2006; Gruber et al., 2008). After fitting the free parameters to one of the experimental stress–strain curves, curves for other film thicknesses and microstructures were predicted and found to be in excellent agreement with the experimental results (Shishvan and Van der Giessen, 2010).

Here, these computations are repeated but for anisotropic grains. A sufficiently long portion of the film with length  $L$  along the  $x_1$  direction is assumed to be subjected to a tensile deformation. The displacement  $u_1$  along the film side edges satisfies

$$\begin{aligned} u_1(0, x_2) &= 0, \\ u_1(L, x_2) &= L\varepsilon(t), \end{aligned} \quad (18)$$

where  $\varepsilon(t)$  is the imposed overall strain as a function of time. Traction free conditions are imposed on the top and bottom surfaces of the film as well as on the right and left edges in  $x_2$  direction, i.e.

$$\begin{aligned} t_i(x_1, 0) &= t_i(x_1, h) = 0, \quad (i = 1, 2), \\ t_2(0, x_2) &= t_2(L, x_2) = 0. \end{aligned} \quad (19)$$

To prevent extensive bending of the film due to nonuniform plastic deformation, the following condition is imposed along the mid-plane of the film,

$$u_2(x_1, h/2) = 0. \quad (20)$$

The details of the superposition method for solving this thin film problem are shown in Fig. 7, with explicit illustration of the boundary conditions for DD and FE sub-problems. Each DD sub-problem is solved according to Fig. 5b. The finite element mesh of the DD sub-problem coincides with the mesh of the FE sub-problem. The traction  $T_i^*$  can then be calculated as the internal nodal forces along the  $S_b$ . An integration method is obviously needed to compute the nodal forces, which has to be done with care in view of the stress singularity carried with each dislocation. Since the accurate computation of these nodal forces plays an important role in the present superposition scheme, two measures are taken: (a) trapezoidal integration is adopted; (b) the obstacles which mimic the impenetrable GB are placed inside the grains at a small distance from the GB. The latter reduces the stress level at the edges of the DD sub-problems (which coincide with GBs) caused by the dislocation pile-ups against these boundaries. This offset is akin the finite thickness of the GBs, and is determined in such a way as to ensure sufficiently accurate calculation of nodal forces. In this study, we have used an offset of  $0.01 \mu\text{m}$ , small enough to only affect the simulation results of very thin/small grain size films.

#### 4.2. Numerical results

The method is applied to the Cu films studied experimentally by Xiang and Vlassak (2006) using plane-strain bulge testing. Material

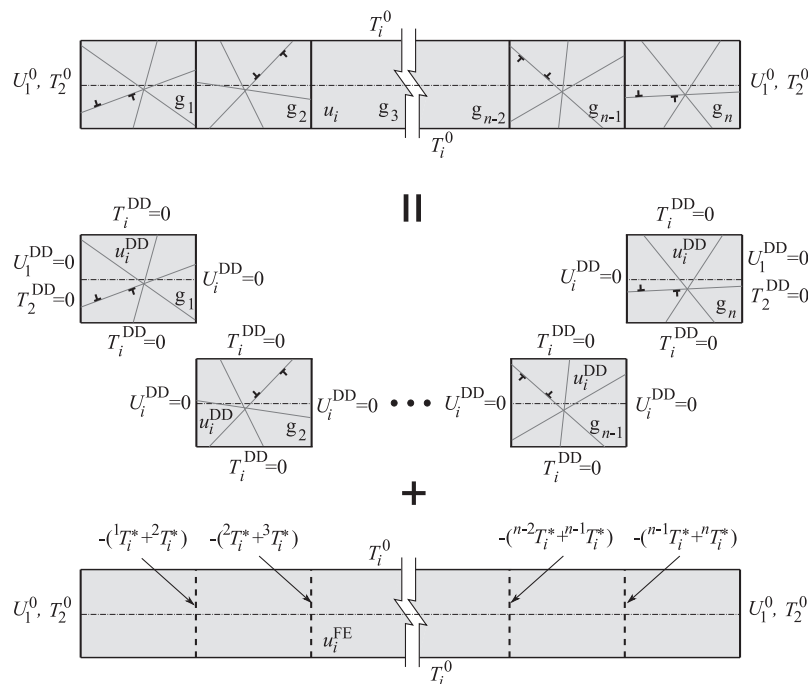
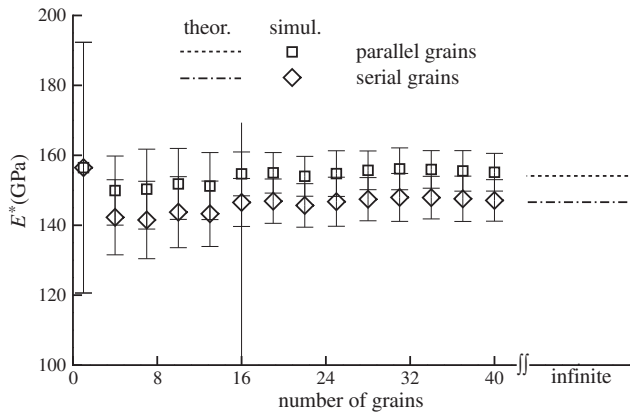


Fig. 7. Schematic description of the superposition technique for solving a thin film.



**Fig. 8.** Plane-strain elastic modulus of a polycrystalline film,  $E^*$ , as a function of the number of grains in the 2D model compared with the theoretical values as presented in Appendix C.

parameters of Cu are  $b = 0.25$  nm and  $B = 10^{-4}$  Pa s with the elastic constants presented in Section 2.1. The nucleation parameters –  $\rho_{\text{nuc}}$  and  $\tau_{\text{nuc}}$  – are the only remaining free material parameters. Values fitted to the experiments by Xiang and Vlassak (2006) are  $\tau_{\text{nuc}}^0 = 0.43 \times 10^{-3} E$  and  $\rho_{\text{nuc}} = 30 \mu\text{m}^{-2}$  (Shishvan and Van der Giessen, 2010). It is worth emphasizing, however, that the model needs  $\rho_{\text{nuc}} \propto 1/d$  for different film thickness/grain size and that the value for  $\rho_{\text{nuc}}$  mentioned above was fitted for a 1  $\mu\text{m}$  thickness film with grain size of  $d = 1.5 \mu\text{m}$ . The reader is referred to (Shishvan and Van der Giessen, 2010) for further details.

A total of 16 grains are used in the computational cell (cf. also Section 4.2.1), and are all assumed to be initially stress free and dislocation free, as in (Nicola et al., 2006; Shishvan and Van der Giessen, 2010). To reduce the statistical effects of orientation, various realizations of grain orientation, source locations and random source strengths are considered for each film thickness and grain size. The corresponding results are averaged and the scatter caused by different realizations is shown as an error bar. Generally, the number of required realizations is chosen such that adding a new realization result yields a negligible change to the averaged response.

#### 4.2.1. Plane-strain elastic modulus

Contrary to the situation of isotropic elasticity, the representation of anisotropy needs careful consideration of the fact that, now, the overall elastic response is also a function of the number of grains in the unit cell. In Appendix C, the anisotropy-dependence of the plane-strain elastic modulus ( $E^*$ ) of a single crystal film is investigated; accordingly the average value of  $E^*$  for an infinitely long polycrystalline film is computed for two idealized cases, where grains are connected either in parallel or in series. Simulations of films containing a finite number of grains reveal that by increasing the number of grains, the values of  $E^*$  converge to the theoretical values (see Appendix C), as shown in Fig. 8 for both cases. For each specific number of grains, ten realizations have been averaged and the associated scatter has defined the error bars. It can be concluded that using 16 grains is a good compromise between computational cost and accuracy (in terms of reduced scatter and close approximation of the theoretical average values).

It is noted that the computed plane-strain elastic modulus (also cf. Appendix C) is larger than the experimental value reported by Xiang et al. (2006) and Gruber (2007), namely 124 ~ 135 GPa (Young's modulus 110 ~ 120 GPa, if  $\nu = 0.34$ ). This difference is mainly attributed to the GBs having a higher compliance than the crystallites. A simple way to remedy the modulus deficit is as follows. By assuming a spring with normalized stiffness  $E_d^*$ , which

is connected in series to a film with plane-strain modulus  $E_f^*$ , the equivalent plane-strain modulus  $E^*$  is given by

$$\frac{1}{E^*} = \frac{1}{E_f^*} + \frac{1}{E_d^*}. \quad (21)$$

The value of  $E_d^*$  is determined by matching the value of  $E^*$  with the experimental data. Solving Eq. (21) for  $E_d^*$ ,

$$E_d^* = \frac{E^* E_f^*}{E_f^* - E^*}. \quad (22)$$

Since the spring is mechanically connected in series to the film, the value of the stress (force) in the spring is equal to the average stress in the film. Therefore, in the present incremental approach, this spring can be easily introduced by modifying the applied displacement (i.e. Eq. (18)<sub>2</sub>) in each time step into

$$u_1(L, x_2) = L \left( \varepsilon(t) - \frac{\sigma(t - \Delta t)}{E_d^*} \right), \quad (23)$$

where  $\sigma(t - \Delta t)$  is the average tensile stress,

$$\sigma = \frac{1}{hL} \int_0^h \int_0^L \sigma_{11}(x_1, x_2) dx_1 dx_2, \quad (24)$$

computed at the previous time step.

#### 4.2.2. Computational issues and predictions of size effects

Beside the incorporation of anisotropic elasticity, the method described in Section 4.1 has certain similarities to the previous study (Shishvan and Van der Giessen, 2010), but also some notable differences in the way the BVP is solved: namely the absence of periodicity in the computational cell and the use of the O'Day and Curtin (2004) superposition method instead of the standard superposition method of Van der Giessen and Needleman (1995). We first explicate the deviations in predictions due to these computational differences by considering the response of a film comprising elastically isotropic grains.

First let us consider the mere effect of the absence of periodic boundary conditions on the cell. Fig. 9 shows predicted stress-strain curves for two films with thicknesses 1.0 and 0.61  $\mu\text{m}$ . The curves labeled “standard- PBC” are from (Shishvan and Van der Giessen, 2010) and are obtained by imposing tension through a prescribed displacement difference between cells of length  $L$ , i.e.  $u_1(L, x_2) = u_1(0, x_2) + L\varepsilon(t)$ , while the ones denoted by “standard-No PBC” are obtained by way of the boundary conditions (18) used here. Since the computational cell includes 16 grains for proper sampling of different grain orientations and source distribution, the influence of the non-periodic boundary conditions is negligible especially for the 1.0  $\mu\text{m}$  thick film.

Fig. 9 also shows the results of the present superposition method. It is observed that these results are in good agreement with the results of the standard method. For thinner films, a higher hardening rate is predicted which can only be related to the position of GB obstacles, which are modeled in a distance 0.01  $\mu\text{m}$  from their original location. Since the plastic behavior is obviously size dependent, this offset decreases the length of slip planes and consequently affects the size dependence. Yet, taking the scatter band into consideration, we conclude that the present superposition method does not influence the results.

It has thus been demonstrated that the present superposition method is well capable of simulating isotropic cases. One advantage of this method over the standard one is its relatively low computational costs, as already emphasized by O'Day and Curtin (2004). To apply a strain of 0.005, the method is 4 ~ 5 times faster, and this gain increases with increasing number of grains in the computational cell and with further straining. The reason lies in

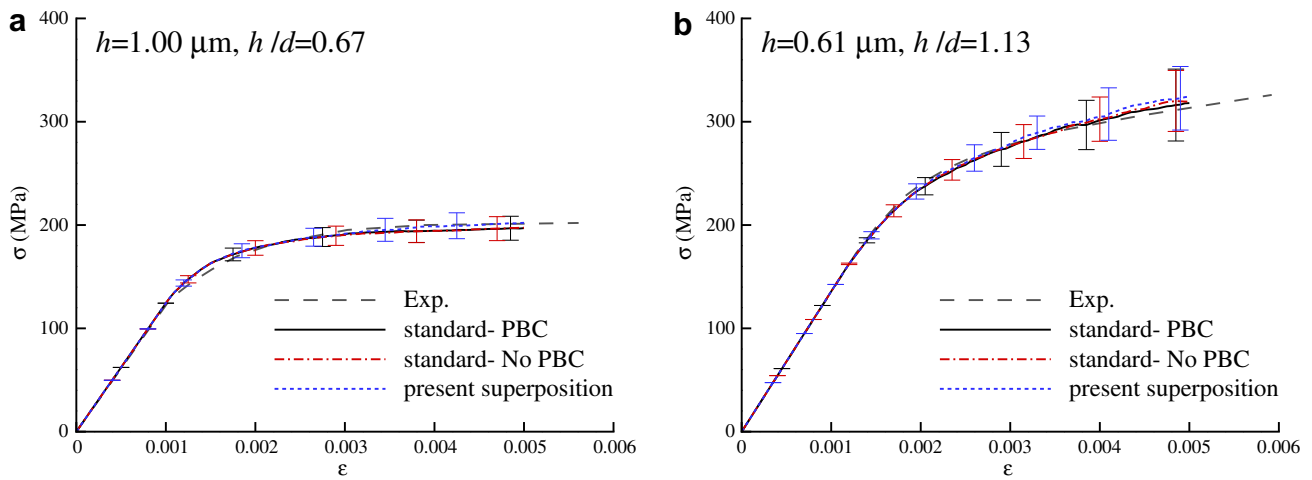


**Fig. 9.** Comparison of stress–strain curves for unpassivated films with elastically isotropic grains predicted with different solution methods: the standard DDP method with a periodic computational cell (indicated by “standard- PBC”) and with a non-periodic cell (denoted by “standard- No PBC”), and by the method described in Section 4.1. The experimental stress–strain curves are from (Xiang and Vlassak, 2006).

the long-range interactions between dislocations: in the standard method the interactions among all dislocations in the film are computed, while in the present approach this is limited to the dislocations in each grain and the remaining ones are transmitted through the boundary tractions  $T_i^*$ .

Now, the results of the 2D DDP method based on anisotropic elasticity are presented. Fig. 10 shows the predicted stress–strain curves for the same two thin films. As was mentioned in Section 4.2.1, the model predicts a higher value for the plane-strain elastic modulus. This is revealed in Fig. 10 for the cases denoted by “anisotropic- unfitted  $E^*$ ”, where the overall elastic modulus is the unbiased prediction on the basis of the cubic elastic constants. The use of Eq. (23), mimicking the influence of the GBs, to prescribe tension allows the experimental value of  $E^*$  to be reproduced by proper fitting of  $E_d^*$ . With all other material parameters being the same as in the isotropic cases, the resulting predictions labeled “anisotropic” exhibit a slightly higher hardening rate, especially for the thinnest film, Fig. 10b. A fraction of this is associated with the numerical technique, as seen in Fig. 9b, but the major part is to be attributed to the higher value of the resolved shear stress of dislocations in the aniso-

tropic model (cf. Fig. 4). The back stress on sources due to the dislocations delays further nucleation of the sources; since the source parameters were fitted by the isotropic model, these effects were not incorporated but would be if this fitting would be done using elastic anisotropy.

#### 4.2.3. Bauschinger effect

2D DDP simulations have recently been employed by Shishvan et al. (2010) to analyse the Bauschinger effect (BE) in unpassivated thin films. It has been shown that the BE has various possible origins: dislocation pile-ups against GBs; constraints on the grain level by neighboring grains; variations in grain orientation; and polydispersity of the grain size. All of these affect the level of stress inhomogeneity inside the films; it is this inhomogeneity that eventually is the driving force for the BE. An issue which has not been considered in the previous study, however, is the elastic stress inhomogeneity in the grain level due to the variation in film texture. To study this contribution we now adopt the present anisotropic DDP model of thin films.

Following Shishvan et al. (2010), an affine deformation assumption on the grain level is adopted as a crude way to augment the 2D

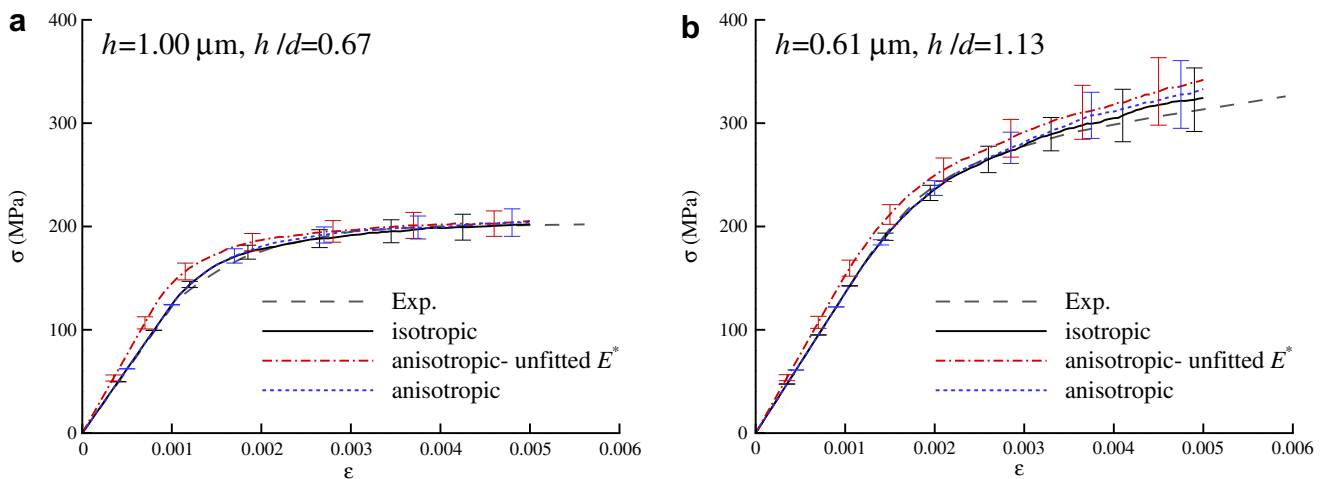


**Fig. 10.** Predicted stress–strain curves for two unpassivated films, using the method described in Section 4.1 with and without fitting the value of  $E^*$  with the experimental data, in comparison with the results of the isotropic model. The experimental data are from Xiang and Vlassak (2006).

framework with the effect of the three dimensional film micro-structure. The interaction between grains in the third dimension is taken into account in an approximate manner by requiring all grains in 2D to co-deform with the others. This so-called *constrained model* imposes the following constraint along the centers of the GBs:

$$u_1\left(jd, \frac{h}{2}\right) = jd\left(\varepsilon(t) - \frac{\sigma(t - \Delta t)}{E_d^*}\right), \quad j = 1, 2, \dots, 15 \quad (25)$$

(note that 16 grains are used in the computational cell). This constraint per grain is easily implemented owing to the superposition method chosen here. If adaptation of  $E^*$  to the experimental data is not considered, the right hand side of Eq. (25) is simply substituted with  $jd\varepsilon(t)$ .

The constrained model generally predicts a higher hardening rate than the unconstrained model with the same parameter values, so that the values provided in the previous subsection cannot be used directly. Instead, we employ the fitting procedure of Shishvan and Van der Giessen (2010) to find free parameters  $-\tau_{nuc}^0$  and  $\rho_{nuc}$  again: for a film with  $h = 1 \mu\text{m}$  and  $d = 1.5 \mu\text{m}$ , the free parameters are  $\tau_{nuc}^0 = 0.52 \times 10^{-3}E$  and  $\rho_{nuc} = 60 \mu\text{m}^{-2}$ . The stress–strain responses, using the constrained model by both isotropic assumption and anisotropy, are shown in Fig. 11a. Adopting

these parameter values, the predicted stress–strain curves of unpassivated films with a thickness of 0.61 and 0.34  $\mu\text{m}$  are shown in Fig. 11b and c, where a very good agreement with experimental data is observed. The anisotropic constrained model predicts a slightly higher hardening rate compared with the isotropic assumption for thinner films, similar to the unconstrained model of Section 4.2.2.

The responses of these films during unloading from two values of pre-strain are also shown in Fig. 11, where there is no significant change in the predicted Bauschinger strain  $\varepsilon_B$ , as defined in Fig. 11b, after incorporation of elastic anisotropy. The Bauschinger strain is often plotted as a function of either the applied pre-strain  $\varepsilon_0$  or the ratio  $(\sigma_{max} - \sigma_1)/E^*$ . Here,  $\sigma_{max}$  is the value of applied pre-stress and  $\sigma_1$  is the elastic limit stress, defined as the point in the stress–strain curve where the secant modulus is equal to 95% of the plane-strain elastic modulus  $E^*$ . Fig. 12a shows the variation of  $\varepsilon_B$  as a function of the pre-strain  $\varepsilon_0$ , both normalized with the yield strain  $\varepsilon_y$  ( $\varepsilon_y = \sigma_y/E^*$ ,  $\sigma_y$  is the yield stress at 0.2% plastic strain offset), computed for unloading from pre-strains of  $\varepsilon_0 = 0.005$  and 0.01. It is clear that there is little or no change in the BE by introducing anisotropic elasticity. Similar conclusions are obtained from Fig. 12b, which presents the variations of the predicted  $\varepsilon_B$  as a function of  $(\sigma_{max} - \sigma_1)/E^*$ .

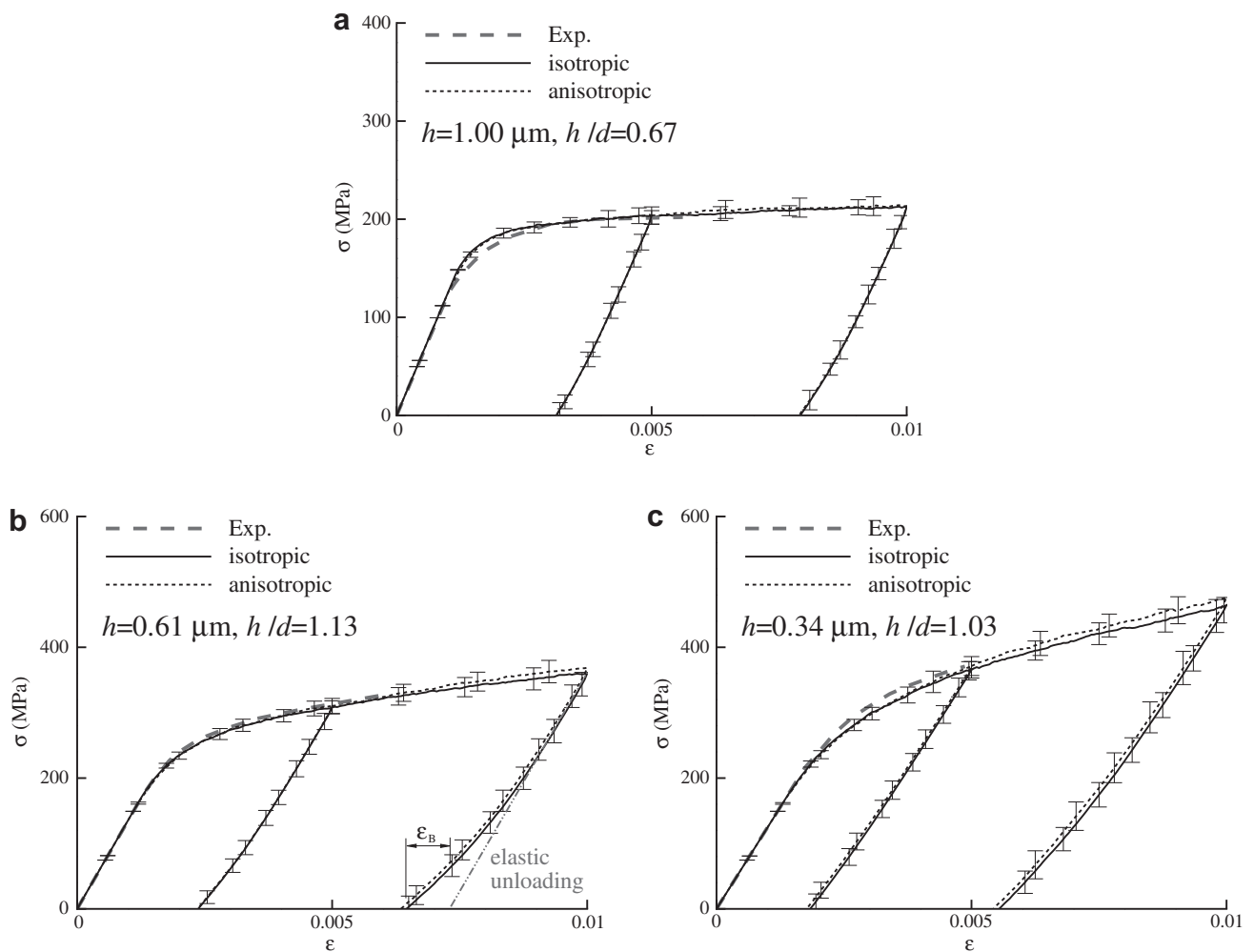


Fig. 11. Loading–unloading responses of unpassivated thin films using the constrained isotropic and anisotropic model compared with the experimental tests of Xiang and Vlassak (2006). In (b), the Bauschinger strain  $\varepsilon_B$  is defined as the difference between the actual residual strain and the hypothetical residual strain if unloading were purely elastic.

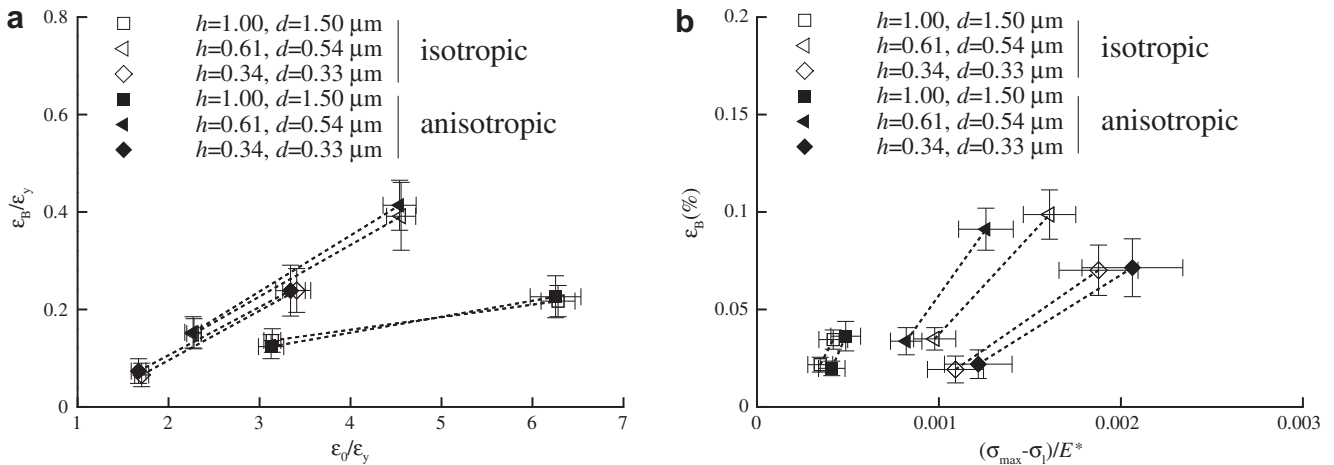


Fig. 12. Variations of  $\epsilon_B$  as a function of (a) pre-strain  $\epsilon_0$  (both normalized by the yield strain  $\epsilon_y$ ), and (b)  $(\sigma_{max} - \sigma_1)/E^*$  by using the constrained model for unpassivated films unloaded from  $\epsilon_0 = 0.005$  and  $\epsilon_0 = 0.01$ .

### 5. Concluding remarks

A two-dimensional discrete dislocation plasticity method (2D DDP) based on anisotropic elasticity has been developed, where the plane-strain plastic deformation of the crystal is achieved by using the effective slip systems introduced by Rice (1987). The superposition method of O'Day and Curtin (2004) has been employed to solve the boundary value problem of a polycrystalline medium.

As a first application, the method has been used to simulate thin copper films. First, by assuming isotropy, the framework has been validated against prior DDP results on thin films. Then, predictions of the size dependent plastic behavior and the Bauschinger effect (BE) have been carried out for anisotropic columnar-grained unpassivated thin films with varying thickness/grain size. Comparisons with the isotropic case have revealed that anisotropy results in slightly higher rate of hardening while the BE is not influenced. This conclusion emphasizes that, even though thin films have strong texture, it is other mechanisms such as dislocations piling-up against grain boundaries, constraints on the grain level by neighboring grains, variations in grain orientation and polydispersity of the grain size that control the BE in unpassivated thin films, as demonstrated in Shishvan et al. (2010).

It bears emphasis that 2D DDP involves several approximations and, for quantitative confrontation with experiments, necessitates a fitting procedure to determine the parameter values for a specific material. Part of the underlying assumptions are associated with the interactions between dislocations and grain boundaries, which includes storage, transmission and nucleation. Each of these mechanisms depends sensitively on the material as well as on the grain-to-grain misorientation. Constitutive rules for these mechanisms are under development but not available at the moment. Therefore, many DDP studies of polycrystals during the last few years—including Nicola et al. (2006), Kumar et al. (2009), Shishvan and Van der Giessen (2010)—have assumed that grain boundaries are impenetrable. As they have been able to predict, for instance, the Hall–Petch effect (Balint et al., 2008), we feel comfortable in making the same assumption here. One should also realize, however, that grain boundary effects may be implicitly included in the fitted values of the source density and source strength, cf. (Shishvan and Van der Giessen, 2010). When, in reality, a grain boundary is permeable to a certain extent, the associated softening will be picked up through an enhanced source density. Other dislocation-grain boundary interactions will be ‘hidden’ in the material parameters as well, thus emphasizing the need for improved constitutive rules to make these interactions explicit in DDP models.

In addition to improvement of the grain boundary modeling, the present anisotropic DD model can be refined in a various aspects. The currently used properties of the 2D sources, such as strength and nucleation time, are based on estimates from isotropic 3D dislocation models (see e.g. Shishvan et al. (2008) and references therein). These could be improved based on elastically anisotropic dislocation simulations in 3D. Furthermore, the constitutive rules can be extended with dynamic sources and obstacles of the type proposed by Benzerga et al. (2004) to account for dislocation interactions in three dimensions.

The observed low sensitivity of thin film behavior to elastic anisotropy is intimately related to the fact that this pertains to the overall response, averaging over many grains. Therefore, we also do not expect a significant effect of elastic anisotropy on the Hall–Petch effect as studied through standard DD by Balint et al. (2008). On the other hand, in view of the fact that elastic anisotropy does affect the plasticity produced by individual dislocations, it is to be expected that phenomena taking place at the size scale of grains or smaller (such as fracture, e.g. Göken et al. (2002)) will depend on the local anisotropy.

### Acknowledgments

S.S.S. gratefully acknowledges financial support from the Ministry of Science, Research and Technology of Iran for his scholarship at the University of Groningen.

### Appendix A. Details of displacement field calculations

It should be emphasized that the direct use of Eq. (3) will not generate the correct discontinuity of the displacement field of an edge dislocation. To clarify the issue assume a dipole where its dislocations have Burgers vectors  $\mathbf{b} = [\pm b \ 0 \ 0]^T$  and are located at  $x = \pm 1$  (Fig. 13). The displacement field  $u_x$  (normalized with  $b$ ) computed directly from Eq. (3)<sub>1</sub> is shown in Fig. 13a, where the displacement jump of  $b$  is not over the slip system that the dipole resides on. To get the correct displacement field, by owing the following arithmetical relation, i.e.

$$\tan^{-1} \alpha + \tan^{-1} \beta = \begin{cases} \tan^{-1} \frac{\alpha + \beta}{1 - \alpha\beta}, & (\alpha\beta < 1), \\ \pi + \tan^{-1} \frac{\alpha + \beta}{1 - \alpha\beta}, & (\alpha > 0, \alpha\beta > 1), \\ -\pi + \tan^{-1} \frac{\alpha + \beta}{1 - \alpha\beta}, & (\alpha < 0, \alpha\beta > 1), \end{cases}$$

it is illustrated that the term  $\tan^{-1} \frac{2xy \sin \varphi}{x^2 - y^2}$  in Eq. (3)<sub>1</sub> should be rewritten in the form of:

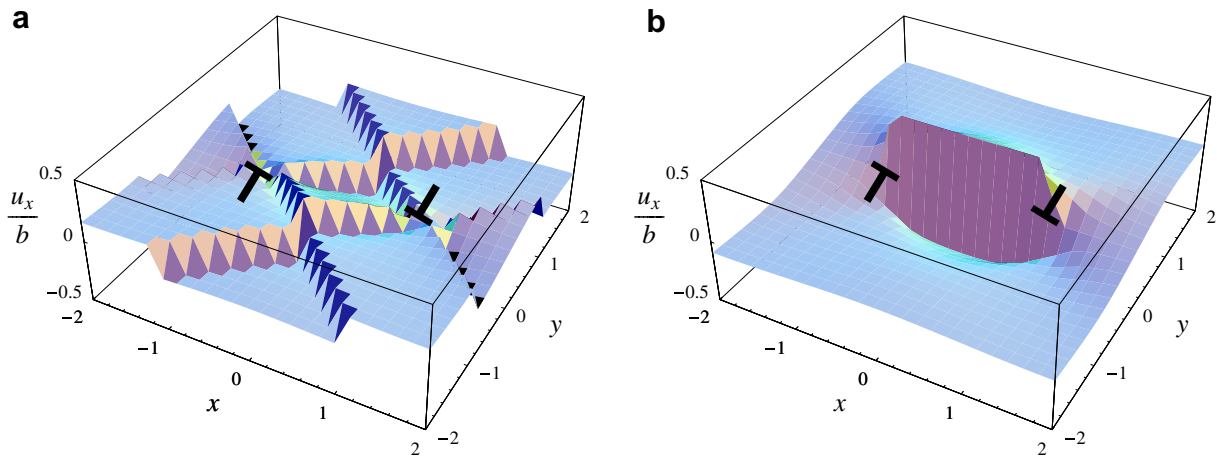


**Fig. 13.** The displacement field  $u_x$  (normalized with  $b$ ) of a dipole where its dislocations have Burgers vectors  $\mathbf{b} = [\pm b \ 0 \ 0]^T$  and are located at  $x = \pm 1$ , (a) computed directly from Eq. (3)<sub>1</sub> and (b) computed from Eqs. (3)<sub>1</sub> and (A.1).

$$\tan^{-1} \frac{2xy\lambda \sin \phi}{x^2 - \lambda^2 y^2} \equiv - \left( \tan^{-1} \frac{x + y\lambda \cos \phi}{y\lambda \sin \phi} + \tan^{-1} \frac{x - y\lambda \cos \phi}{y\lambda \sin \phi} \right). \quad (\text{A.1})$$

Fig. 13b shows the displacement field  $u_x$  (normalized with  $b$ ) computed from Eqs. (3)<sub>1</sub> and (A.1), which shows the correct discontinuity in the displacement field.

Similarly, the term  $\tan^{-1} \frac{2xy\lambda \sin \phi}{x^2 - \lambda^2 y^2}$  in Eq. (3)<sub>2</sub> should be re-written as:

$$\tan^{-1} \frac{2xy\lambda \sin \phi}{x^2 - \lambda^2 y^2} \equiv - \left( \tan^{-1} \frac{x \cos \phi - y\lambda}{x \sin \phi} - \tan^{-1} \frac{x \cos \phi + y\lambda}{x \sin \phi} \right), \quad (\text{A.2})$$

where the following relations are accordingly used.

$$\tan^{-1} \alpha - \tan^{-1} \beta = \begin{cases} \tan^{-1} \frac{\alpha - \beta}{1 + \alpha\beta}, & (\alpha\beta > -1), \\ \pi + \tan^{-1} \frac{\alpha - \beta}{1 + \alpha\beta}, & (\alpha > 0, \alpha\beta < -1), \\ -\pi + \tan^{-1} \frac{\alpha - \beta}{1 + \alpha\beta}, & (\alpha < 0, \alpha\beta < -1), \end{cases}$$

$$\tan^{-1} \frac{\gamma}{\omega} = \begin{cases} \frac{\pi}{2} - \tan^{-1} \frac{\omega}{\gamma}, & (\gamma\omega > 0), \\ -\frac{\pi}{2} - \tan^{-1} \frac{\omega}{\gamma}, & (\gamma\omega < 0). \end{cases}$$

## Appendix B. Orientation-dependent elastic constitutive law for plane strain

Each grain in the polycrystal has a different orientation with respect to the global  $x_1 - x_2$  coordinate system, see Fig. 5. This orientation is defined as the angle  $\phi$  between the  $x$  axis of the plane-strain coordinate system of crystal and the  $x_1$  axis of global coordinate system, as shown in Fig. 14.

Generally, the fields in the global coordinate system are of interest. Yet, the displacement and stress fields of dislocations are calculated best first in the  $x-y$  coordinate system (see Fig. 1b and Fig. 14) based on the closed-form expressions (3)–(5). The desired fields in the  $x_1 - x_2$  system are obtained subsequently by transformation rules. For the finite element solution (to enforce boundary conditions in the superposition framework), however, it is easier to directly establish the anisotropic constitutive law in the global reference frame. For a grain with orientation  $\phi$  in the plane-strain condition, it can be written in contracted notation as:

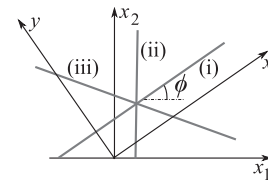


**Fig. 14.** The global coordinate system  $x_1 - x_2$  and the plane-strain  $x-y$  axes with slip systems (see Fig. 1b); the in-plane angle  $\phi$  defines the orientation.

$$\begin{Bmatrix} \sigma_{11} \\ \sigma_{22} \\ \sigma_{12} \end{Bmatrix} = \begin{bmatrix} C_{11} & C_{12} & C_{16} \\ C_{12} & C_{22} & C_{26} \\ C_{16} & C_{26} & C_{66} \end{bmatrix} \begin{Bmatrix} \varepsilon_{11} \\ \varepsilon_{22} \\ 2\varepsilon_{12} \end{Bmatrix}, \quad (\text{B.1})$$

where

$$\begin{aligned} C_{11} &= c'_{11} \cos^4 \phi + 2(c'_{12} + 2c'_{66}) \cos^2 \phi \sin^2 \phi + c'_{22} \sin^4 \phi, \\ C_{22} &= c'_{22} \cos^4 \phi + 2(c'_{12} + 2c'_{66}) \cos^2 \phi \sin^2 \phi + c'_{11} \sin^4 \phi, \\ C_{12} &= \frac{1}{8} [c'_{11} + 6c'_{12} + c'_{22} - 4c'_{66} - (c'_{11} - 2c'_{12} + c'_{22} - 4c'_{66}) \cos 4\phi], \\ C_{16} &= \frac{1}{4} [c'_{11} - c'_{22} + (c'_{11} - 2c'_{12} + c'_{22} - 4c'_{66}) \cos 2\phi] \sin 2\phi, \\ C_{26} &= -\frac{1}{4} [-c'_{11} + c'_{22} + (c'_{11} - 2c'_{12} + c'_{22} - 4c'_{66}) \cos 2\phi] \sin 2\phi. \end{aligned} \quad (\text{B.2})$$

## Appendix C. Elastic response of thin films

Fig. 15 depicts a single crystal film with the crystal orientation  $\phi$  under plane-strain tension. Note that the  $x_3$  axis is the direction of plane-strain condition of film. The elastic stiffness of the film depends on the orientation  $\phi$ . Using the Hooke's law in terms of the compliances, Young and plane-strain elastic modules can be written as:

$$E = S_{1111}^{-1},$$

$$E^* = \left( S_{1111} - \frac{S_{1133}^2}{S_{3333}} \right)^{-1}. \quad (\text{C.1})$$

Compliances  $S_{ijkl}$  are defined in the global coordinate system  $x_1 - x_2$ , and require two transformations; first, the compliances in the coordinate system  $x-y$  are defined from the compliances in the crystal

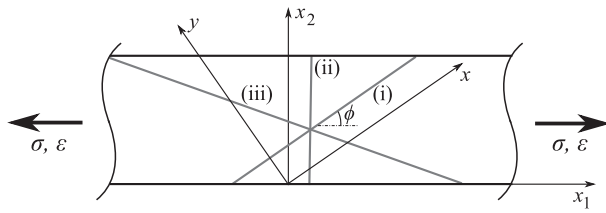


Fig. 15. A single crystal film under plane-strain tension.

Table C.1

Computed values of Young and plane-strain elastic modules for different textures.

Texture	Tensile direction	$\phi$	$E$ (GPa)	$E^*$ (GPa)
{101}	(010)	90°	66.0	101.0
{010}	(101)	0°	130.6	133.0
{111}	(121)	54.74°	130.6	174.7
{121}	(111)	35.26°	191.6	201.6
{023}	(232)	46.69°	164.6	198.9

It is worth noting that while the values of  $E$  and  $E^*$  depend on the tensile direction, but these values for {111} texture are independent of the tensile direction. The  $\langle 010 \rangle$  (i.e.  $\phi = 90^\circ$ ) directions have the minimum value of Young's modulus,  $E$ , while the  $\langle 111 \rangle$  directions (i.e.  $\phi = 35.264^\circ$ ) have the maximum  $E$ , both in agreement with available data (e.g. Reid, 1973). The computed values of Young and plane-strain elastic modules for a number of textures are listed in Table C.1.

The elastic response of a polycrystalline thin film, consisted of different grains with different orientations, depends on the interaction of grains. Two limit cases can be considered, they are either mechanically connected in series or in parallel. The former results in the same stress state while the latter gives rise to the same straining. In a real film, the texture of the film can be measured and the total elastic behavior of the film can be evaluated by assuming either of these two cases (Xiang et al., 2006; Gruber, 2007). Here, if the same probability (uniform distribution for  $\phi$ ) is assumed for all orientations (say  $\phi$  in the present 2D framework) then,

a. parallel grains:

$$\begin{aligned} \bar{E}_p &= \frac{2}{\pi} \int_0^{\frac{\pi}{2}} E(\phi) d\phi = 131.6 \text{ GPa}, \\ \bar{E}_p^* &= \frac{2}{\pi} \int_0^{\frac{\pi}{2}} E^*(\phi) d\phi = 154.1 \text{ GPa}, \end{aligned} \quad (C.5)$$

b. serial grains:

$$\begin{aligned} \bar{E}_s &= \left( \frac{2}{\pi} \int_0^{\frac{\pi}{2}} \frac{1}{E(\phi)} d\phi \right)^{-1} = 116.4 \text{ GPa}, \\ \bar{E}_s^* &= \left( \frac{2}{\pi} \int_0^{\frac{\pi}{2}} \frac{1}{E^*(\phi)} d\phi \right)^{-1} = 146.6 \text{ GPa}. \end{aligned} \quad (C.6)$$

Average values of these bounds provide good estimates for the Young and plane-strain elastic modules of the polycrystalline thin film, i.e.  $E \sim 124$  Gpa and  $E^* \sim 150$  GPa, comparable to the experimental value of the Young's modulus for polycrystalline copper: 122.5 GPa (Reid, 1973).

(cubic) coordinate system, and second, these are transformed to the global coordinate system. The results are:

$$\begin{aligned} E &= \left[ s'_{11} \cos^4 \phi + 2(s'_{12} + 2s'_{66}) \cos^2 \phi \sin^2 \phi + s'_{22} \sin^4 \phi \right]^{-1}, \\ E^* &= \left[ s'_{11} \cos^4 \phi + 2(s'_{12} + 2s'_{66}) \cos^2 \phi \sin^2 \phi + s'_{22} \sin^4 \phi \right. \\ &\quad \left. - \frac{(s'_{13} \cos^2 \phi + s'_{12} \sin^2 \phi)^2}{s'_{33}} \right]^{-1}. \end{aligned} \quad (C.2)$$

Here, similar to Eq. (2),  $s'_{ij}$  are compliances in the coordinate system  $x$ - $y$ ,

$$\begin{aligned} s'_{11} &= \frac{1}{2}(s_{11} + s_{12} + 2s_{44}), \\ s'_{22} &= s_{11}, \\ s'_{33} &= \frac{1}{2}(s_{11} + s_{12} + 2s_{44}), \\ s'_{12} &= s_{12}, \\ s'_{13} &= \frac{1}{2}(s_{11} + s_{12} - 2s_{44}), \\ s'_{66} &= s_{44}, \end{aligned} \quad (C.3)$$

where  $s_{ij}$  are the elastic compliances in the crystal coordinate system,

$$\begin{aligned} s_{11} &= \frac{c_{11} + c_{12}}{c_{11}^2 + c_{11}c_{12} - 2c_{12}^2}, \\ s_{12} &= \frac{-c_{12}}{c_{11}^2 + c_{11}c_{12} - 2c_{12}^2}, \\ s_{44} &= \frac{1}{4c_{44}}. \end{aligned} \quad (C.4)$$

Fig. 16 shows the variation of Young and plane-strain elastic modules, Eq. (C.2), as a function of the crystal orientation  $\phi$  for copper. It is clearly observed that there is a symmetry with respect to  $\phi = 90^\circ$ . It should be noted that this 2D model does not consider all possible 3D orientations, because the tensile direction is restricted to the {101} plane (see Figs. 15 and 1).

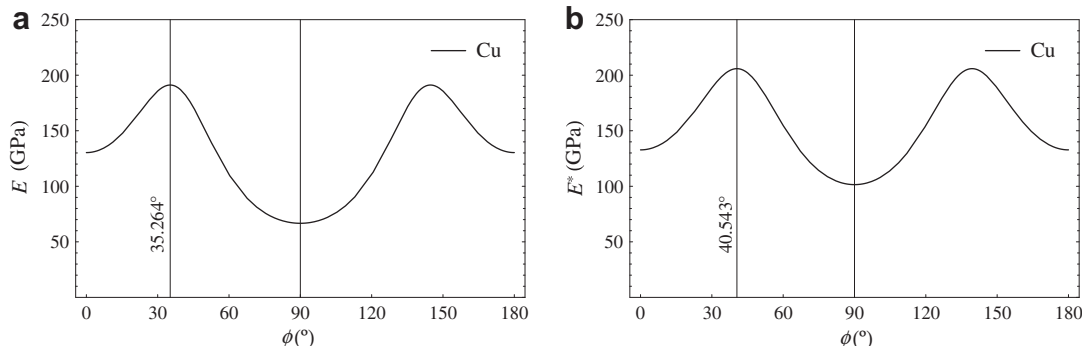


Fig. 16. (a) Young's modulus of elasticity,  $E$  and (b) plane-strain elastic modulus,  $E^*$ , as functions of crystal orientation  $\phi$ , see Fig. 15.

## References

- Acharya, A., Bassani, J.L., 2000. Lattice incompatibility and a gradient theory of crystal plasticity. *J. Mech. Phys. Solids* 48, 1565–1595.
- Bacon, D.J., Barnett, D.M., Scattergood, R.O., 1980. Anisotropic continuum theory of lattice defects. *Prog. Mater. Sci.* 23, 51–262.
- Baker, S.P., Kretschmann, A., Arzt, E., 2001. Thermomechanical behavior of different texture components in Cu thin films. *Acta Mater.* 49, 2145–2160.
- Balint, D.S., Deshpande, V.S., Needleman, A., Van der Giessen, E., 2008. Discrete dislocation plasticity analysis of the grain size dependence of the flow strength of polycrystals. *Int. J. Plast.* 24, 2149–2172.
- Benzerger, A.A., Brechet, Y., Needleman, A., Van der Giessen, E., 2004. Incorporating three-dimensional mechanisms into two-dimensional dislocation dynamics. *Model. Simul. Mater. Sci. Eng.* 12, 159–196.
- Cleveringa, H.H.M., Van der Giessen, E., Needleman, A., 1997. Comparison of discrete dislocation and continuum plasticity predictions for a composite material. *Acta Mater.* 45, 3163–3179.
- Cleveringa, H.H.M., Van der Giessen, E., Needleman, A., 2000. A discrete dislocation analysis of mode I crack growth. *J. Mech. Phys. Solids* 48, 1133–1157.
- Deshpande, V.S., Needleman, A., Van der Giessen, E., 2002. Discrete dislocation modeling of fatigue crack propagation. *Acta Mater.* 50, 831–846.
- Eshelby, J.D., Read, W.T., Shockley, W., 1953. Anisotropic elasticity with applications to dislocation theory. *Acta Met.* 1, 251–259.
- Fleck, N.A., Hutchinson, J.W., 2001. A reformulation of strain gradient plasticity. *J. Mech. Phys. Solids* 49, 2245–2271.
- Göken, M., Thome, F., Vehoff, H., 2002. Study of crack tip deformation in FeAl and NiAl crystals with optical interference microscopy and atomic force microscopy. *Phil. Mag.* A 82, 3241–3250.
- Gruber, P.A., 2007. Mechanical Properties of Ultra Thin Metallic Films Revealed by Synchrotron Techniques. Ph.D. thesis, Universität Stuttgart.
- Gruber, P.A., Böhm, J., Onuseit, F., Wanner, A., Spolenak, R., Arzt, E., 2008. Size effects on yield strength and strain hardening for ultra-thin Cu films with and without passivation: a study by synchrotron and bulge test techniques. *Acta Mater.* 56, 2318–2335.
- Gurtin, M.E., 2002. A gradient theory of single-crystal viscoplasticity that accounts for geometrically necessary dislocations. *J. Mech. Phys. Solids* 50, 5–32.
- Guruprasad, P.J., Carter, W.J., Benzerger, A.A., 2008. A discrete dislocation analysis of the Bauschinger effect in microcrystals. *Acta Mater.* 56, 5477–5491.
- Han, X., Ghoniem, N.M., Wang, Z., 2003. Parametric dislocation dynamics of anisotropic crystals. *Phil. Mag.* 83, 3705–3721.
- Hirth, J.P., Lothe, J., 1982. *Theory of Dislocations*, second ed. Wiley, New York.
- Kubin, L.P., Canova, G., Condat, M., Devincere, B., Pontikis, V., Brechet, Y., 1992. Dislocation microstructures and plastic flow: a 3D simulation. *Solid State Phenomena* 23/24, 455–472.
- Kumar, R., Nicola, L., Van der Giessen, E., 2009. Density of grain boundaries and plasticity size effects: a discrete dislocation dynamics study. *Mater. Sci. Eng. A* 527, 7–15.
- Kysar, J.W., Gan, Y.X., Morse, T.L., Jones, X.C.M.E., 2007. High strain gradient plasticity associated with wedge indentation into face-centered cubic single crystal: geometrically necessary dislocation densities. *J. Mech. Phys. Solids* 55, 1554–1573.
- Kysar, J.W., Gan, Y.X., Mendez-Arzuza, G., 2005. Cylindrical void in a rigid-ideally plastic single crystal. Part I: anisotropic slip line theory solution for face-centered cubic crystals. *Int. J. Plast.* 21, 1481–1520.
- Limkumnerd, S., Van der Giessen, E., 2008. Study of size effects in thin films by means of a crystal plasticity theory based on DiFT. *J. Mech. Phys. Solids* 56, 3304–3314.
- Liu, Z.L., Zhuang, Z., Liu, X.M., Zhao, X.C., Zhang, Z.H., 2010. A dislocation dynamics based higher-order crystal plasticity model and applications on confined thin-film plasticity. *Int. J. Plast.* doi:10.1016/j.ijplas.2010.04.004.
- Nicola, L., Van der Giessen, E., Gurtin, M.E., 2005a. Effect of defect energy on strain-gradient predictions of confined single-crystal plasticity. *J. Mech. Phys. Solids* 53, 1280–1294.
- Nicola, L., Van der Giessen, E., Needleman, A., 2003. Discrete dislocation analysis of size effects in thin films. *J. Appl. Phys.* 93, 5920–5928.
- Nicola, L., Van der Giessen, E., Needleman, A., 2005b. Size effects in polycrystalline thin films analyzed by discrete dislocation plasticity. *Thin Solid Films* 479, 329–338.
- Nicola, L., Xiang, Y., Vlassak, J.J., Van der Giessen, E., Needleman, A., 2006. Plastic deformation of freestanding thin films: experiments and modeling. *J. Mech. Phys. Solids* 54, 2089–2110.
- O'Day, M.P., Curtin, W.A., 2004. A superposition framework for discrete dislocation plasticity. *J. Appl. Mech.* 71, 805–815.
- Rajagopalan, J., Han, J.H., Saif, M.T.A., 2008. Bauschinger effect in unpassivated freestanding nanoscale metal films. *Scr. Mater.* 59, 734–737.
- Reid, C.N., 1973. *Deformation Geometry for Materials Scientists*. Pergamon Press, Oxford.
- Rhee, M., Stolken, J.S., Bulatov, V.V., de la Rubia, T.D., Zbib, H.M., Hirth, J.P., 2001. Dislocation stress fields for dynamic codes using anisotropic elasticity: methodology and analysis. *Mater. Sci. Eng. A* 309–310, 288–293.
- Rice, J.R., 1987. Tensile crack tip fields in elastic-ideally plastic crystals. *Mech. Mater.* 6, 317–335.
- Shishvan, S.S., Mohammadi, S., Rahimian, M., 2008. A dislocation-dynamics-based derivation of the Frank-Read source characteristics for discrete dislocation plasticity. *Model. Simul. Mater. Sci. Eng.* 16, 075002. 17pp.
- Shishvan, S.S., Nicola, L., Van der Giessen, E., 2010. Bauschinger effect in unpassivated freestanding thin films. *J. Appl. Phys.* 107, 093529. 9pp.
- Shishvan, S.S., Van der Giessen, E., 2010. Distribution of dislocation source length and the size dependent yield strength in freestanding thin films. *J. Mech. Phys. Solids* 58, 678–695.
- Van der Giessen, E., Needleman, A., 1995. Discrete dislocation plasticity: a simple planar model. *Model. Simul. Mater. Sci. Eng.* 3, 689–735.
- Wang, Y., Kysar, J.W., Vukelic, S., Yao, Y.L., 2009. Spatially resolved characterization of geometrically necessary dislocation dependent deformation in microscale laser shock peening. *J. Manuf. Sci. Eng.* 131, 041014-1-9.
- Widjaja, A., Needleman, A., Van der Giessen, E., 2007. The effect of indenter shape on sub-micron indentation according to discrete dislocation plasticity. *Model. Simul. Mater. Sci. Eng.* 15, S121–S131.
- Widjaja, A., Van der Giessen, E., Needleman, A., 2005. Discrete dislocation modelling of submicron indentation. *Mater. Sci. Eng. A* 400, 456–459.
- Xiang, Y., Tsui, T.Y., Vlassak, J.J., 2006. The mechanical properties of freestanding electroplated Cu thin films. *J. Mater. Res.* 21, 1607–1618.
- Xiang, Y., Vlassak, J.J., 2006. Bauschinger and size effects in thin-film plasticity. *Acta Mater.* 54, 5449–5490.
- Yin, J., Barnett, D.M., Cai, W., 2010. Efficient computation of forces on dislocation segments in anisotropic elasticity. *Model. Simul. Mater. Sci. Eng.* 18, 045013. 14pp.